



Photocatalytic activity of iron oxide nanoparticles synthesized by different plant extracts for the degradation of diazo dyes Evans blue and Congo red

Souhaila Meneceur^{1,2} · Hadia Hemmami^{1,2} · Abderrhmane Bouafia^{1,2}  · Salah Eddine Laouini^{1,2} · Mohammed Laid Tedjani^{1,2} · Djamilia Berra^{1,2} · Mohammed Sadok Mahboub³

Received: 1 February 2022 / Revised: 19 April 2022 / Accepted: 23 April 2022 / Published online: 5 May 2022
© The Author(s), under exclusive licence to Springer-Verlag GmbH Germany, part of Springer Nature 2022

Abstract

This work describes the use of XRD, SEM, and infrared spectroscopy in the evaluation of iron oxide nanoparticles as produced from three distinct plant extracts. The efficacy of the nanoparticles in terms of dye sorption was assessed using Congo Red (CR) and Evans Blue (EB) dyes. The research revealed that the synthesis method influences the properties of nanoparticles, which leads to different levels of effectiveness when it comes to sorption. The proposed sorption mechanism was founded on several characterization studies. Moreover, it was discovered that sorption might occur due to pores or binding groups rather than only an electrostatic connection. The results show that the nanoparticles' sorption effectiveness is heavily pH dependent. The produced nanoparticles showed potential for application in water treatment technologies due to the synthetic technique relative ease and the possibility of a low-cost catalyst.

Keywords Iron oxide nanoparticles · Congo red · Evans Blue · Photosynthesis · Catalytic Activity · Dye degradation

1 Introduction

The rapid expansion of the industrial sector causes a greater amount of dye waste-water to be released directly into the natural environment, and by extension, it comes with several ramifications on human health. [1] Congo Red (CR) and Evans Blue (EB) are benzidine-based anionic diazo dyes characterized by two azo linkages ($-N=N-$) chromophores [2]. They are commonly utilized in textiles, medicines, paper industries, and ink manufacturing, among several other applications. [3] Because the dye molecule is so stable, natural decomposition is extremely difficult. As a result, purification is critical for its elimination so that pollution of

the environment may be averted. [4] The contaminated water has higher concentrations of Chemical Oxygen Demand and Biochemical Oxygen Demand, as well as substantial amounts of suspended particles and other contaminants. Consequently, peculiar procedures in the treatment of discharged wastewater are required.

Several conventional physical and chemical methods such as coagulation, reverse osmosis, chemical oxidation, adsorption, and catalytic and photocatalytic degradation have been utilized for removal of the dye effluents [5, 6]. Among these, photocatalysis is one of the most effective, low-cost, and safe techniques for successful degradation of organic pollutants and dyes under ambient temperature and pressure [7, 8]. Heterogeneous photocatalysis is an efficient technology to remove environmental pollutants in natural sources. Heterogeneous photocatalysis can be described as the acceleration of photoreaction in the presence of a catalyst [9].

Globally, nanomaterials are subject to intensive studies in recent years due to their inherent high surface area properties [10], namely, increased catalysis, adsorption capabilities, and high reactivity [8, 11]. A wide variety of nanoparticles were used successfully for treatment of different contaminants including CuO [12], Silver-doped ZnO [13], TiO₂ [14], and Au [15]. Lately, with the increasing importance of

✉ Abderrhmane Bouafia
abdelrahmanebouafia@gmail.com

¹ Department of Process Engineering and Petrochemistry, Faculty of Technology, University of Echahid Hamma Lakhdar El Oued, 39000 El Oued, Algeria

² Laboratoire de Biotechnologie Biomatériaux Et Matériaux Condensés, faculté de la technologie, Université Echahid Hammam Lakhdar, El Oued, Algeria

³ LEVRES Laboratory, University of El Oued, 39000 El Oued, Algeria

nano-technology, iron oxide nanoparticles have been extensively studied and used for the removal of organic [16, 17].

Various iron oxide nanoparticles, in particular, have unique qualities and are used in a variety of disciplines of science and technology, including data storage, dye degradation, drug delivery systems, magnetic resonance imaging, waste water treatment, environmental bioremediation, and more [18–20].

As a result, the synthesis of different iron oxides at the nanoscale level has been a hot topic of research across the world. Iron oxides are a type of transition metal oxide with the unusual attribute of having a colorful appearance and a poor solubility [21].

Antiferromagnetic hematite (Fe_2O_3), paramagnetic, ferromagnetic, ferromagnetic maghemite, supermagnetic magnetite (Fe_3O_4), and orthorhombic structure are all examples of iron oxides found in nature. The most frequent Fe minerals were magnetite, hematite, and maghemite (III) [22, 23]. In the synthesis of diverse forms of iron oxides, many process factors such as precursor concentrations, temperature, and medium pH play a critical role [20, 24].

When compared to other nanoparticles, iron oxide nanoparticles (Fe_3O_4 NPs) have low toxicity, biocompatibility, cost-effectiveness, and a high surface area to volume ratio [23, 25, 26].

Using various plant extracts, this work proposes an effective and sustainable strategy for the biosynthesis of (Fe_3O_4) nanoparticles from aqueous ferric chloride (FeCl_3). The influence of average crystallite size/precursor concentrations (volume ratios percent v/v) on Fe_3O_4 NP formation, the optical characteristics, as well as catalytic activity toward the degradation of CR and EB dyes were examined in our work. CR and EB dyes were picked for this research due to them being the most used azo dyes in the textile industry. Benzidine, a human carcinogen, and mutagen, is known to be metabolized from this family of colors. Due to it being structurally stable and severely toxic, its use is prohibited in many countries around the world [27]. In this work, the biodegradable and detoxifying effects of Fe_3O_4 NPs on the breakdown of CR and EB dyes at various reaction periods are investigated.

2 Experimental section

2.1 Materials

The materials used are ferric chloride (FeCl_3 , 98%) and hydrochloric acid (HCl) were purchased from Sigma-Aldrich Germany, distilled water. As for the green synthesis of iron oxide, we used the leaf extracts of *Mentha Pulegium L.*, *Artemisia herba-alba Asso.*, and the fruit peels of *Punica Granatum L.* These materials were harvested at El-Oued

region (South-East of Algeria; 33° 07 '00" N 7° 11 '00 "E). Our selection is based on studies conducted in the VTRS laboratory. They were used to synthesize iron oxide NPs. *LOBA CHEMIE*, India supplied the CR and MB dyes.

2.2 Plant extract preparation

Leaves of *Mentha Pulegium L.*, and *Artemisia herba-alba* were harvested during March 2019. The fruit peels of *Punica Granatum L.* were obtained in September 2019 from local farms in El Oued region (south-eastern Algeria). The fresh leaves and the fruit peel were then washed and dried at room temperature, in shade for 7–12 days. They were protected from sunlight in order to preserve the integrity of their chemical composition, before being crushed so that a fine powder may be obtained.

For the extraction of phytochemicals, we chose the technique of extraction by maceration in water-during which the solid is placed for a longer or shorter period in a liquid. By putting together 10 g of powdered solid plant material (leaves or fruit peel) and 100 ml of distilled water in a 250-ml glass beaker, the extract was made. The mixture was then stirred on a regular basis for 24 h at room temperature. It was after that filtered using filter paper (Whatman No: 42), and stored in an airtight glass container at 4° C for later use.

2.3 Biosynthesis of iron oxide nanoparticles

Iron oxide nanoparticles were synthesized via the reduction of iron ions in ferric chloride (FeCl_3) solution by phenolic compounds from plant extracts (Fig. 1).

A modified technique from earlier studies [28–36] was used to make iron oxide magnetite (Fe_3O_4) nanoparticles. Briefly stated, by adding a concentration of 0.1 M of the solution of ferric chloride (FeCl_3) to the extract following a volume ratio of 1:10 (v / v) between extract and ferric chloride, we ended up with 20 ml / 200 ml in a 250-ml beaker. The reduction process allowed us to immediately obtain iron oxide nanoparticles. The mixture is stirred continuously at 75° C for 1 h. A change of color from light brown to dark black indicates the formation of iron oxide NPs. The mechanism of formation is explained by the reduction of iron ions that takes place with the phenolic compounds in the plant extract.

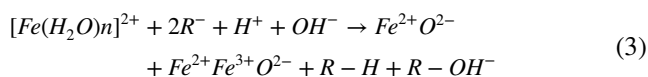
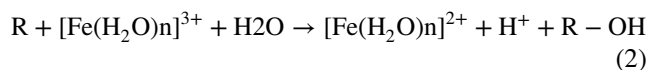
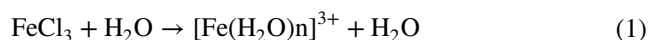
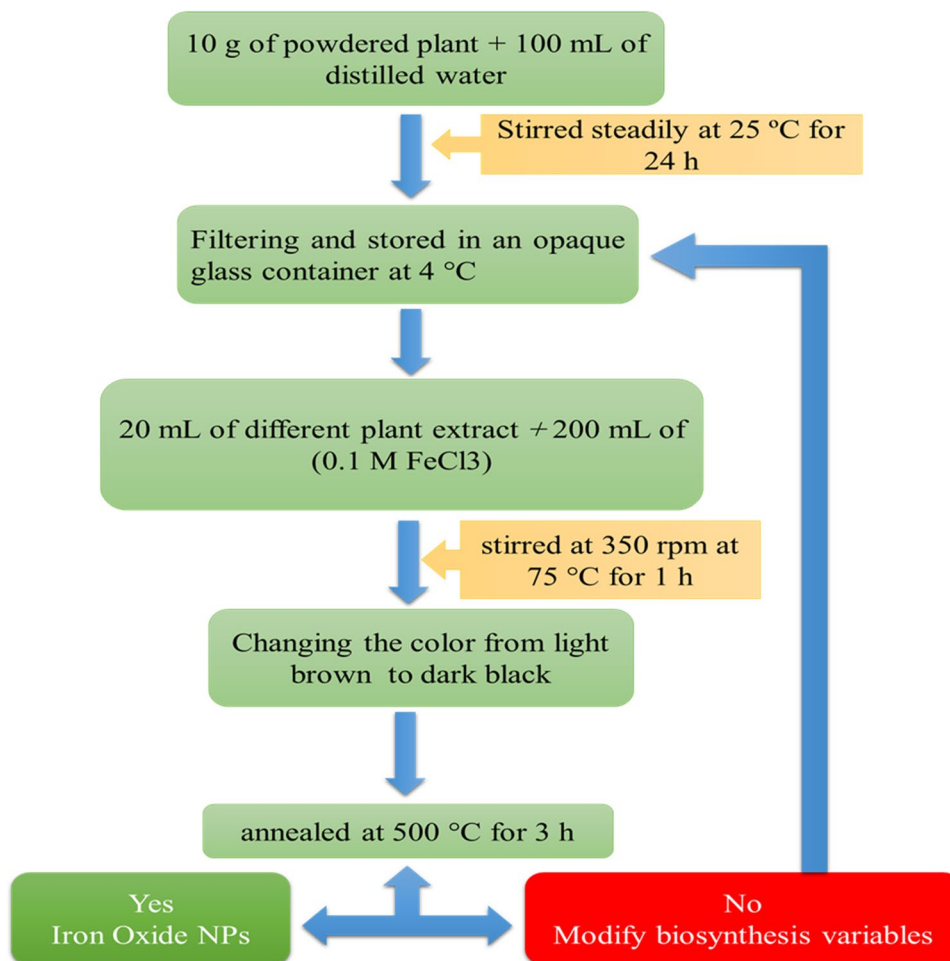


Fig. 1 Flow chart for green synthesis of iron oxide NPs by different plant extracts



A small amount of the synthesized iron oxide NPs solution was saved for UV–visible measurements.

Centrifugation at 3000 rpm for 15 min allowed us to collect the solid product. The synthesized NPs samples were washed in distilled water several times, then dried in a drying oven at 100° C for 24 h. To completely crystallize the NPs and get rid of the organic compounds of the plant extract, the dry powder was annealed at 500° C for 3 h in an oven. The resulting powders were stored in several containers with different characterizations.

2.4 Characterization of $\text{Fe}_2\text{O}_3/\text{Fe}_3\text{O}_4$ nanoparticles

The characterization of iron oxide nanoparticles relied on the use of the techniques: UV–Vis, FT-IR, DRX, SEM and EDX.

By relying on "Rigaku Miniflex 600" advance diffractometer (Bruker AXS, Karlsruhe, BW, Germany) in a 2θ range of 20–70°, we managed to conduct the X-ray analysis of distinct mixed solids. At 40 kV and 40 mA with 2 theta° 2 min⁻¹ scanning speeds and Cu Kα radiation, we run the patterns at hand. We also used SEM-TESCAN

VEGA3 Model XMU, LMH (Brno, Czech Republic) for speeding up the voltage of 10 kV in order to capture the Scanning electron microscope (SEM) of iron oxide NPs. Furthermore, a particle disperser unit for the dispersion of individual particles over the SEM setup was deployed. Using the Nicolet iS5 (LLC, Madison, WI USA) Spectrophotometer, the investigated solid's Fourier-transform infrared (FTIR) spectrum, determine the presence of functional groups in leaf extract. At wavelengths between 4000 and 500 cm⁻¹, the optical characteristics of iron oxide NPs were carried out using a UV–Vis spectrophotometer (the device is Shimadzu UV-1800, Japan UV–Vis Spectrophotometer). Data was recorded in the wavelength region of 200 to 900 nm. UV spectrophotometric measurements followed up the green synthesis of iron oxide NPs.

The crystallite size was calculated using the Scherrer formula (Eq. (4)), by selecting the dominating peak of the highest intensity.

$$D = \frac{k\lambda}{\beta\cos\theta} \quad (4)$$

where D is the crystallite size, k is the so-called shape factor (0.9), λ is the wavelength (0.15418 nm, $\text{CuK}\alpha$), β is the Full Width at Half Maximum (FWHM), and θ is the diffraction angle.

2.5 Photocatalytic degradation of Congo Red and Evans Blue

With reactants in both the aqueous phase, i.e. Azo dye in solution, and the solid phase catalyst—iron oxide-NPs—the photocatalytic degradation of dyes is characterized as a heterogeneous catalytic reaction. In the sense that such surface-catalyzed reactions come to pass when there is a reaction between azo dye molecules being adsorbed on the catalyst surface.

Iron oxide NPs were used for catalytic degradation of CR at room temperature. At first, we combined 5 mL of diluted CR, and then analyzed the UV–vis spectroscopy—It peaked at $\lambda_{\text{max}} = 488$ nm. To examine the catalytic impact of iron oxide NPs samples, we added samples of iron oxide NPs (2 mg) to the CR solution (2×10^{-5} M) and adjusted the pH accordingly until the reaction was complete at the volume of 5 mL. With 250–900 nm wavelength at 10–120 min, we kept an eye on the degradation process spectrophotometrically. Decolorization was a decline in the absorbance intensity (λ_{max}) of the solution.

Via measuring Evan's blue dye degradation rate, we could evaluate the catalytic activity of the catalyst. A stock solution of dye (5×10^{-6} M) was prepared by dissolving (1.2 mg) of dye in 250 mL doubly distilled water. pH of the dye solution was measured by a digital pH meter, and the desired pH of the solution (pH = 8) was adjusted by the addition of standard 0.1 M Hydrochloric acid and 0.1 M sodium hydroxide solutions. The reaction mixture containing 2 mg catalyst in 5 mL of solution (Evans Blue). The Centrifugal of solution was used to cut off degradations. The absorbance of the solution was measured at $\lambda_{\text{max}} = 620$ nm [37] at various time (15, 30, 60 and 120 min intervals) was measured with the spectrophotometer.

3 Results and discussion

3.1 Structure and composition properties

The influence of the different plants extracts on the synthesized iron oxide NPs has been studied employing diverse analysis techniques. The mean content of *Mentha pulegium* L. was obtained to be tannins, glycosides, saponins and volatile oils, such as terpenes, alkaloids, phenols and flavones. In the other hand, no resins were noticed for this

plant. Meanwhile the hot ethanolic extract holds all kinds of saponins, glycosides, alkaloids, terpenes, steroids, phenols, volatile oils, tannins, coumarins, flavones except resins [38].

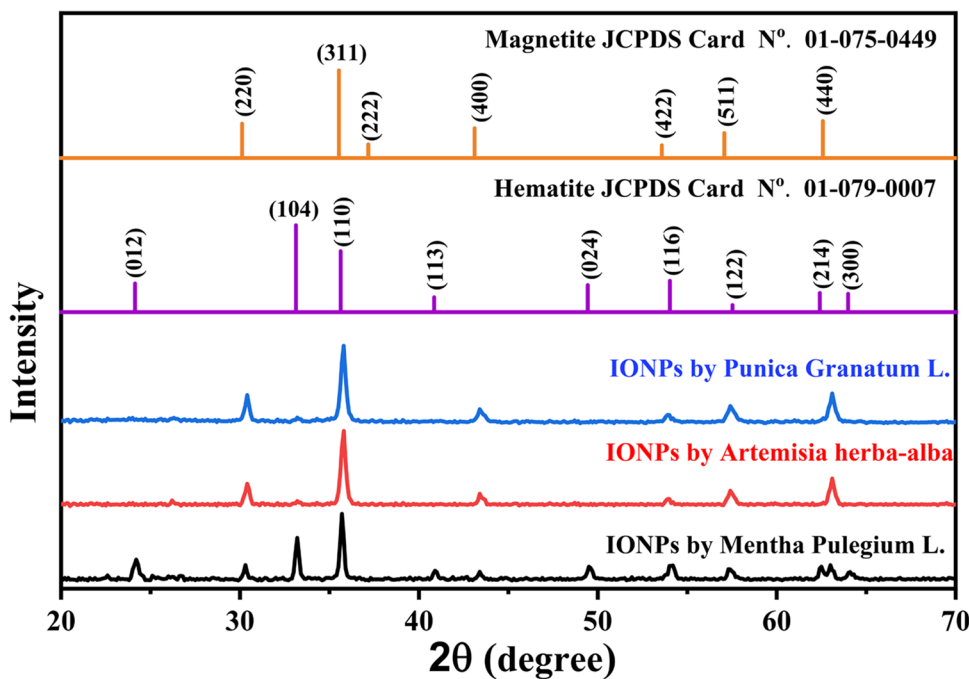
Phytochemical analysis considering *Artemisia* species confirmed that it contain all the classes of phytochemicals in the genus with specific reference to terpenes and flavonoids [39].

Different extracts resulted exploiting different extraction techniques were employed to quantify the condensed tannins, flavonoids and the total phenolic content of *Artemisia Herba-alba*. The different extraction techniques have yielded a total phenolic content of a range between 24.27 and 5.7 mg GAE/g, a content of flavonoid expressed in catechin equivalent is of a range between 10.8 to 16.5 CE/g, and condensed tannins represented in catechin equivalents is of a range between 4.8 to 6.5 mg CE/g. The ultrasonic and conventional extraction techniques were found to have the most significant quantity of anthocyanins, flavonoids, phenolics, and tannins. [40].

Punica granatum L. or the so-called pomegranate is getting increasing interest due to its diverse benefits for human health since it holds a considerable amount of biomolecules, including tannins, flavonoids, and phenolic acids. Which clearly reflected on its production and consumption in the last decades. The results confirmed the presence of all the tested phytochemicals in *P. granatum* peels, excluding glycosides and anthocyanins. Meanwhile all the tested phytochemicals were presented of the ethanol extract of *P. granatum* peels excluding glycosides, tannins and anthocyanins. In the other hand, for the acetone extract of the same plant peels confirmed that it poses all the investigated phytochemicals excluding alkaloids, saponins and anthocyanins [41].

The XRD patterns of IONPs synthesized by different plants are shown in Fig. 2. The patterns indicates that IONPs synthesized by *Artemisia herba-alba* and *Punica Granatum* L. are with single phase shown in Fig. 2 with the peaks located at 2θ positions of 30.2° , 35.4° , 43.2° , 53.34° , 57.3° , and 62.9° linked to (220), (311), (400), (422), (511), and (440) crystal planes of cubic Magnetite (Space Group: P 1 #1–1) with the JCPDS Card No.01–075-0449 [42]. Meanwhile, the XRD pattern of IONPs synthesized by *Mentha Pulegium* L. indicates that it is composed of two phases, (56.4%) Hematite phase distinguished by the peaks centered at 24.13° , 33.15° , 35.45° , 40.70° , 49.47° , 54.04° , 57.50° , 62.90° and 63.98° which correspond to the crystal planes of (012), (104), (110), (113), (024), (116), (122), (214) of rhombohedral crystal structure (Space Group: R -3 c #167–2) with the JCPDS Card No.01–079-0007 [43]. The peaks at 2θ value of 30.25° , 35.45° , 43.20° , 53.60° , 57.26° , and 62.90° , on the other hand, correspond to the planes of (011), (112),

Fig. 2 Iron oxide nanoparticles synthesized XRD patterns



(202), (004), (321), and (224) of cubic Magnetite (Space Group: P 1 #1–1) with the JCPDS Card No.01–075-0449 [42]. The crystallite size was found to differ from a plant to other, where the estimated size of *Mentha Pulegium L.*, *Artemisia herba-alba*, and *Punica Granatum L.* crystallite sizes were 42.37, 31.68, 30.17 respectively Table 1.

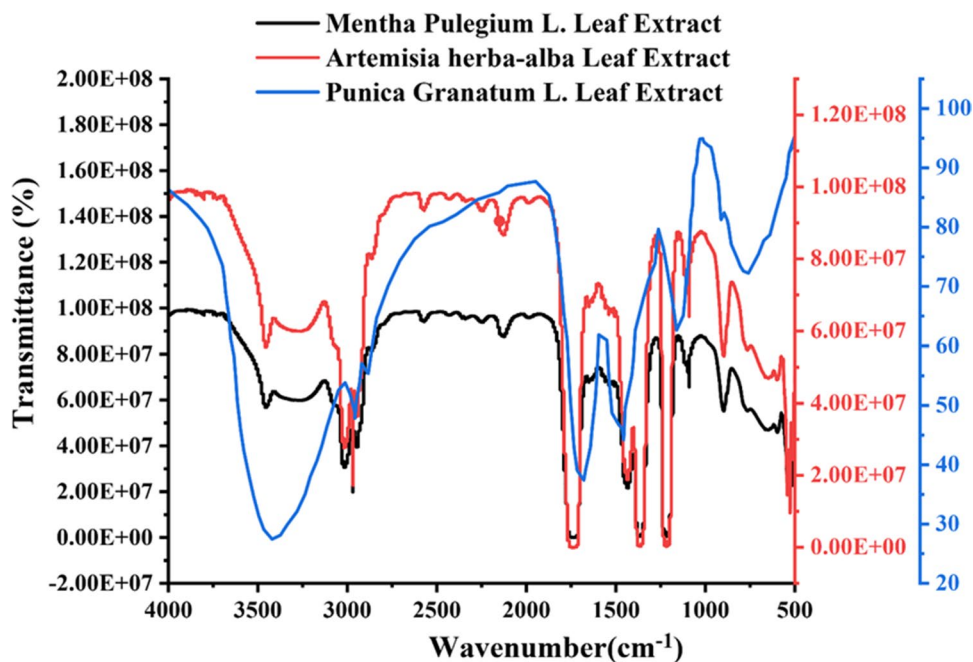
3.2 FTIR spectroscopy analysis

The FTIR spectra of the different plants are shown on Fig. 3. The transmittance plots exhibited several bonds of the diverse functional groups presented on the studied plants extracts.

Table 1 Quantification and average size of iron oxide NPs obtained by different plant extracts

Plant (bioreducer)	Crystallite size	Presented Phases			Lattice parameters	Crystal system	COD Entry	Refs
		Name	Amount(%)	Formula				
<i>Mentha Pulegium L.</i>	42.37 nm	Hematite	56.4	Fe ₂ O ₃	Space Group: R -3 c (#167–2) a=5.43000 Å α=55.2800° b=5.43000 Å β=55.2800° c=5.43000 Å γ=55.2800°	Trigonal (rhombohe- dral axes)	1,011,240	[43]
		Magnetite	43.6	Fe ₃ O ₄	Space Group: P 1 (#1–1) a=8.53335 Å α=90.0000° b=8.53335 Å β=90.0000° c=8.53335 Å γ=90.0000°	Cubic	9,005,841	[42]
<i>Artemisia herba-alba</i>	31.68 nm	Magnetite	100	Fe ₃ O ₄	Space Group: P 1 (#1–1) a=8.53335 Å α=90.0000° b=8.53335 Å β=90.0000° c=8.53335 Å γ=90.0000°	Cubic	9,005,841	[42]
<i>Punica Granatum L.</i>	30.17 nm	Magnetite	100	Fe ₃ O ₄	Space Group: F d -3 m (#227–2) a=8.34400 Å α=90.0000° b=8.34400 Å β=90.0000° c=8.34400 Å γ=90.0000°	Cubic	9,005,841	[42]

Fig. 3 FTIR spectra for the different plant extracts (*Mentha Pulegium L.*, *Artemisia herba-alba* and *Punica Granatum L.*)

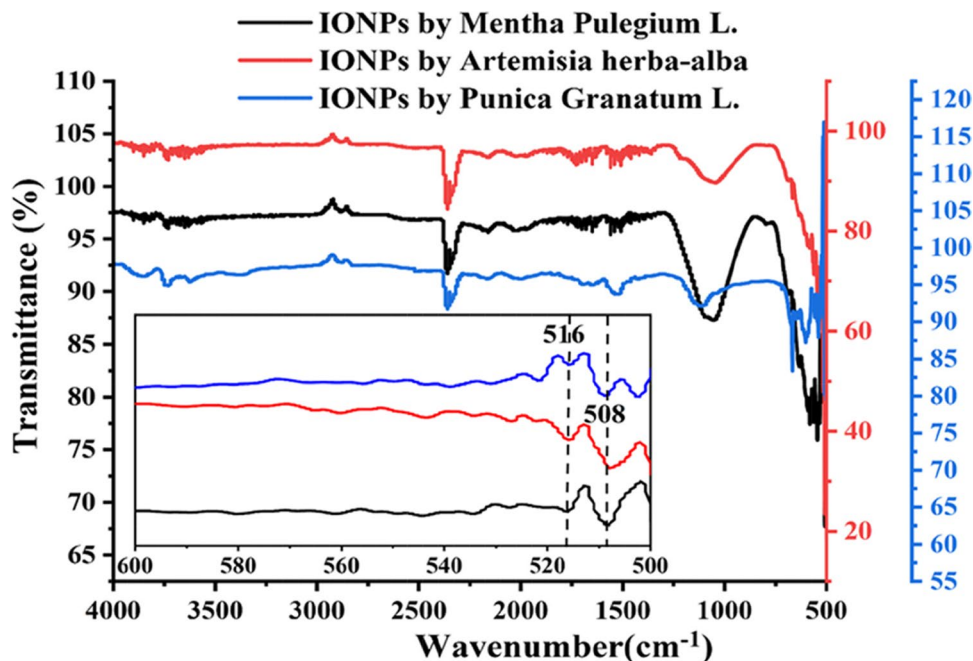


The broad peak around 3500 to 3300 cm^{-1} are allocated to the bond of O–H stretching vibrations [44], C–H both asymmetric and symmetric stretching vibrations was identified by the bonds located at 2911 cm^{-1} and 2840 cm^{-1} respectively [45], the bonds placed around 1650 cm^{-1} and 1450 cm^{-1} are related to the C=O and C=C stretching vibrations respectively [46]. C–N stretching vibration band of amines appears at 1540 cm^{-1} [46]. Also, the two peaks seen at (1235 and 1050) cm^{-1} are attributed to C–O band

stretching and C–OH bending vibrations respectively [47]. These observed on the different FTIR spectra of the different plant extracts indicates that they poses different polyphenolic groups [45], that can play the role of reducing and stabilizing agents for iron oxide nanoparticles biosynthesis [48–53].

The FTIR spectra of iron oxide nanoparticles biosynthesized by different plants is shown in Fig. 4. The peaks centered at 516 cm^{-1} , and 508 cm^{-1} are assigned to the Fe–O

Fig. 4 FTIR spectra of iron oxide nanoparticles synthesized from different plant extracts (*Mentha Pulegium L.*, *Artemisia herba-alba* and *Punica Granatum L.*)



stretching vibrations, similar findings were also observed by prior studies [54, 55]. Comparing the FTIR spectra of the pure plant extract and the biosynthesized IONPs reveals on a remarkable decrease in the hydroxyl group band situated at 3368 cm^{-1} indicates that this functional group was consumed during the biosynthesis process and has played a significant role in reducing and stabilizing IONPs [49, 56].

3.3 Morphological investigation

SEM was employed to investigate the formation of iron oxide nanoparticles and their morphology. The SEM images of the synthesized iron oxide NPs with different plant extracts (*Mentha Pulegium* L., *Artemisia herba-alba*, and the fruit peel of *Punica Granatum* L.) is shown in Fig. 5. The iron oxide NPs were of a majority trend of spherical and oval shapes. Most of the iron oxide NPs were placed as an aggregated form with a minority of dispersed separate particles. The particle size distribution histograms seen in Fig. 5b, d, f indicated that the average size distribution of

the biosynthesized iron oxide NPs is mainly around 70 nm. Given the size of the obtained particles and by comparing them with the size of the crystals, we conclude that the particles are crystals.

Agglomeration of iron oxide nanoparticles is a process that lowers free surface energy by increasing its size and decreasing its surface area. The agglomeration of nanoparticles occurs with the adhesion of the particles to each other through weak forces that lead to (sub) nanoentities [57].

Further analysis of iron oxide nanoparticles, by EDS, as shown in Fig. 6 its associated data, confirms the presence of iron and oxygen, with a weight percentage of approximately 64.35% Fe and 27.16% O.

3.4 Bandgap and optical characteristics

Figure 7b displays the UV–Vis spectra of iron oxide nanoparticles synthesized using the leaves extract of *Mentha Pulegium* L., *Artemisia herba-alba*, and the fruit peels of *Punica Granatum* L. The UV–Vis spectra reveals on

Fig. 5 SEM images and particle size distributions of biosynthesized iron oxide NPs with different plant extracts: (a,b) by *Mentha Pulegium* L., (c,d) by *Artemisia herba-alba*, (e,f) by *Punica Granatum* L.

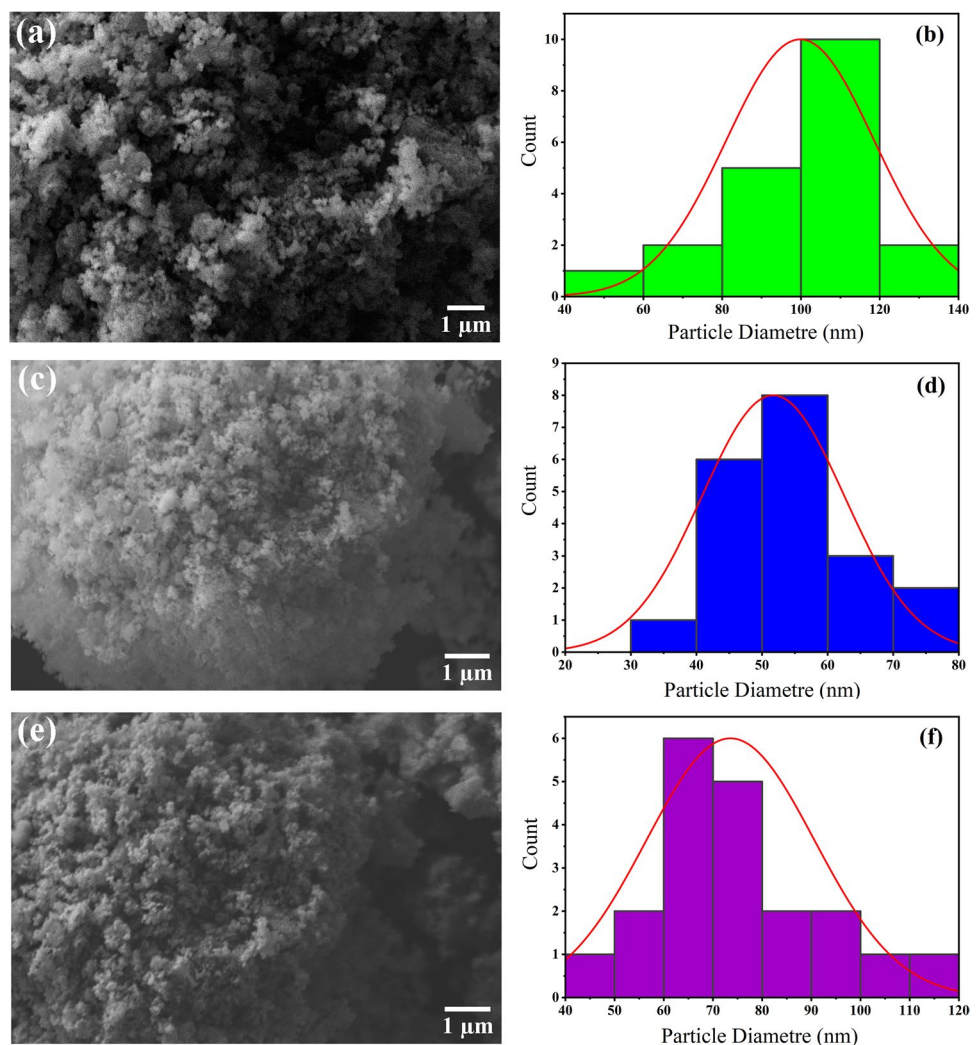
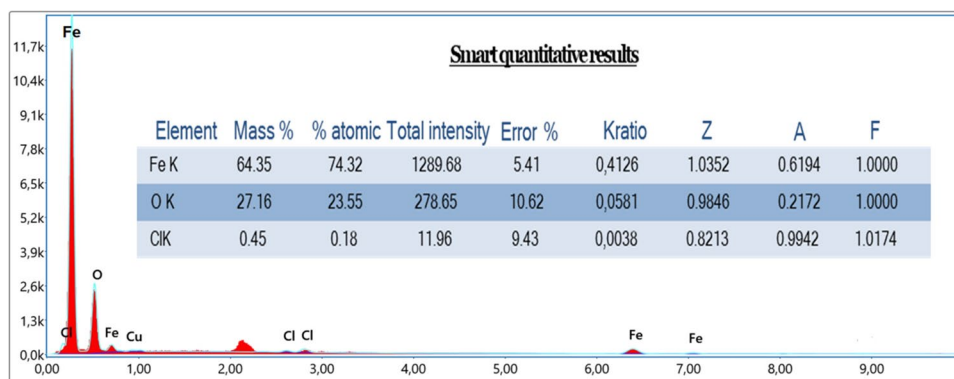


Fig. 6 EDS of iron oxide nanoparticles



a single peak of maximum absorption located around 275–301 nm which can be an indicator for the formation of iron oxide nanoparticles [58, 59]. When the light hits the colloidal iron oxide NPs samples, it leads to its excitation resulting a notable absorption band in the range of the visible light; which take place when the electromagnetic field resonates with the perceived evolution of electrons [60]. The naked eye observation have shown that the color immediately changed from light brown to dark black after mixing plant extracts with precursor, and then it changes gradually to dark brown this color change observed is a sign of the excitation of surface absorption by spectroscopic resonance [61]. The peak intensity has been changed from a plant to other, this may be due to an increase in the number of nanoparticles formed due to transformations of iron ions, which can vary by the different amount of bio-reducing agents presented in each plant, complete docking of them (iron ions) by the extract. The spectra of the three plant extracts showed different peaks shown in Fig. 7a.

Tauc's formula (Eq. 5) was employed to determine the optical band gap (E_g) of iron oxide nanoparticles [62, 63]:

$$(\alpha h\nu)^2 = A(h\nu - E_g) \quad (5)$$

where $h\nu$ is the energy of light, A is constant, α is the absorption coefficient and n is a constant represents the nature of the electron transition, when the transmission is direct $n=2$, and when the transmission is indirect $n=1/2$ [64]. Figure 7c–d shows the plot of $(\alpha h\nu)^2$ and $(\alpha h\nu)^{1/2}$ versus $h\nu$. The gap energy was determined from the intersection of linear section of the absorption spectrum with the axis of energy line. When $(\alpha h\nu)^2$ and $(\alpha h\nu)^{1/2}$ equals to “0”, the photon energy is E_g . The optical band gap of samples is shown in Table 2.

By plotting $(\alpha h\nu)^2$ and $(\alpha h\nu)^{1/2}$ versus photon energy ($h\nu$), the optical energy bandgap for direct E_{g1}^{opt} and indirect E_{g2}^{opt} the transition can be determined, respectively [65, 66].

As per previous studies, direct and indirect energy gap values for the as-synthesized iron oxide NPs samples

brought us a range from 0 to 3 eV [67]. The results are consistent with the literature review suggesting that the bandgap inversely proportional to particle size [65, 68, 69].

$$\ln a = \frac{h\nu}{E_u} + \text{constant}(\ln a_0) \quad (6)$$

Urbach energy denotes the breadth of the localized states' band tails. the Urbach energy E_u can be determined exploiting the slope of the linear section of the graph of $\ln(a)$ versus photon energy Fig. 6e [70]. The different values of the calculated Urbach energy attributed to the different plants are listed in Table 2.

3.5 Photocatalytic activity of iron oxide NPs for azo dye degradation

In Erlenmeyer flasks, 5 mL of dye solution was combined with 2 mg of each the adsorbents.

After that, the mixtures were swirled at a speed of 300 rpm. The samples were taken out and centrifuged after a certain amount of time, and the concentration of dyes in the liquid phase was evaluated using a UV visible spectrophotometer (SHIMADZU 1800) set to 600 nm. The amount of adsorption at equilibrium is calculated through the equation q_e (mg/g):

$$q_e = \frac{(C_0 - C_e)V}{m} \quad (7)$$

With C_0 and C_e (mg/L) representing the initial concentration as well as the equilibrium liquid phase dye concentration. While V stands for the volume of the solution (L), and m represents the mass of adsorbents (g).

Another common reaction to confirm the catalytic activity of iron oxide NPs with EB was the catalytic hydrolysis of the EB dye. UV–vis spectroscopy is used to monitor the stimulation (Fig. 8a,c,e). The dye is catalytically reduced as soon as iron oxide NPs as components are added to the reaction mixture. During the deterioration process, the EB

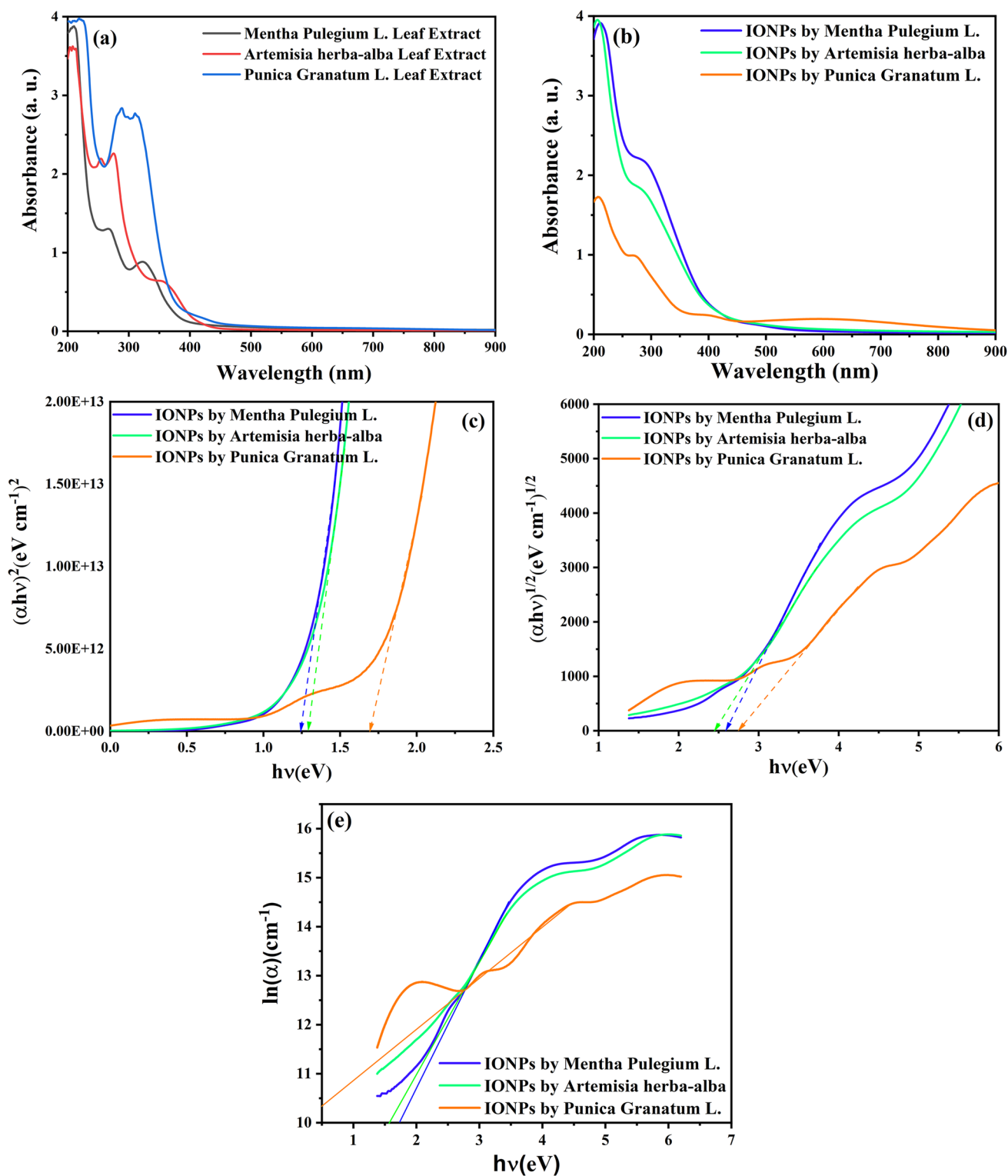


Fig. 7 UV-visible spectra: leaf extract (a) and iron oxide NPs (b); optical energy bandgap for both direct (c) and indirect (d) transitions relying on Tauc’s method; Urbach energy (e)

Table 2 The effect of plant -source on the characteristics of the prepared iron oxide NPs

Samples	Direct bandgap (eV)	Indirect bandgap (eV)	Urbach energy (eV)
IONPs by <i>Mentha Pulegium L</i>	1.23	2.58	0.401
IONPs by <i>Artemisia herba-alba</i>	1.29	2.44	0.456
IONPs by <i>Punica Granatum L</i>	1.67	2.75	0.968

solution's bright blue hue fades and becomes colorless after 8 min. The initial absorption peak at 663 nm progressively faded over time, indicating the composite iron oxide NPs' catalytic activity. Figure 8b shows the computed degradation percentage as a quantitative expression of degraded dyes. Biosynthetic iron oxide NPs increase the reduction process (the dye dissolves faster up to 98% in 10 min).

From Fig. 8, we notice that the adsorption of iron oxide particles synthesized by *Mentha Pulegium L* leaf extract of Evan Bleu was greater over time compared to the adsorption of iron oxide particles synthesized by *Artemisia herba alba asso* leaf extract and *Punica granatum* fruit peel, and this may explain the formation of iron oxide particles synthesized by *Mentha Pulegium L* leaf extract. has two phases, hematite and magnetite.

Upon applying optimal experimental conditions, achieve a 98% degradation rate within 60 min was observed in Fig. 9a–b. The following formula calculates the degradation efficiency [71–74]:

$$\text{Degradation ratio (\%)} = \frac{C_0 - C_t}{C_t} \times 100$$

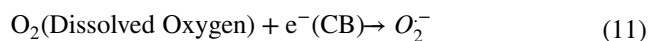
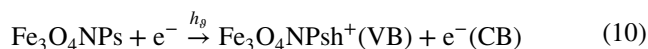
where C_0 is the initial concentration of CR, and C_t is the immediate concentration.

Two phenyl rings are linked to two naphthalene terminal pads that contain amino and sulfonic acids to form CR. CR dye is a carcinogenic metabolite that is used in industries such as paper and elastics, and it induces malignant bladder development in humans. As a result of its high inherent harmfulness, its reduction is a critical concern. Under various testing situations, biosynthetic iron oxide NPs detected the synergist debasement of CR. In the UV–vis region, the CR fluid arrangement exhibits two tops at 340 nm and 490 nm, which correspond to the azo ($-N=N-$) bond. Azo linkages in the color particle break down during the CR lowering measure, producing distinct aromatic amine items (*sodium 4-amino-1-naphthalene sulfonate and 1,1'-Biphenyl*).

IONPs were used for catalytic degradation of CR at room temperature. The sample of iron oxide NPs was chosen

for further photodegradation studies as it shows the best structural and morphological characteristics based on the techniques used. The results further prove that the IONPs catalyst exhibits good photoreactivity, confirming the corresponding degradation efficiency.

A possible mechanism for the deterioration of Evan's blue in the presence of iron oxide NPs has been postulated based on the experimental findings. Evan's blue absorbs light of a sufficient wavelength and, by intersystem crossing, converts to a singlet excited state, then to a triplet excited state (ISC). Furthermore, the semiconductor, when it absorbs light, it causes the excitement of an electron from its valence band (VB) to its conduction band (CB). It is afterwards taken by dissolved oxygen to produce $O_2^{\bullet-}$ (in basic media). These radicals have the ability to breakdown dye to its leuco state, and then to products [75, 76].



In basic medium



The reaction rates were found to be unaffected by the presence of the $\bullet OH$ radical scavenger, 2-propanol. This demonstrates that $\bullet OH$ radicals did not play a role as an active oxidizing species in these processes.

The influence of pH on Evans blue photocatalytic degradation is shown in Fig. 1. The photocatalytic process depends on the dye solution's pH—as observed in the graph [77]. The pH of the solution is changed by adding 0.1 M HCl or 0.1 M NaOH. The rate of deterioration is faster in basic circumstances than in acidic settings. This remark is consistent with the findings reported in [78].

Figure 10 depicts effect of pH on Evans blue photocatalytic degradation. As seen in the graph [77], the photocatalytic process is significantly reliant on the dye solution's pH. Adding 0.1 M HCl or 0.1 M NaOH to the solution changes the pH. In basic conditions, the pace of degradation is faster than in acidic conditions. This in particular is in agreement with the findings in [79].

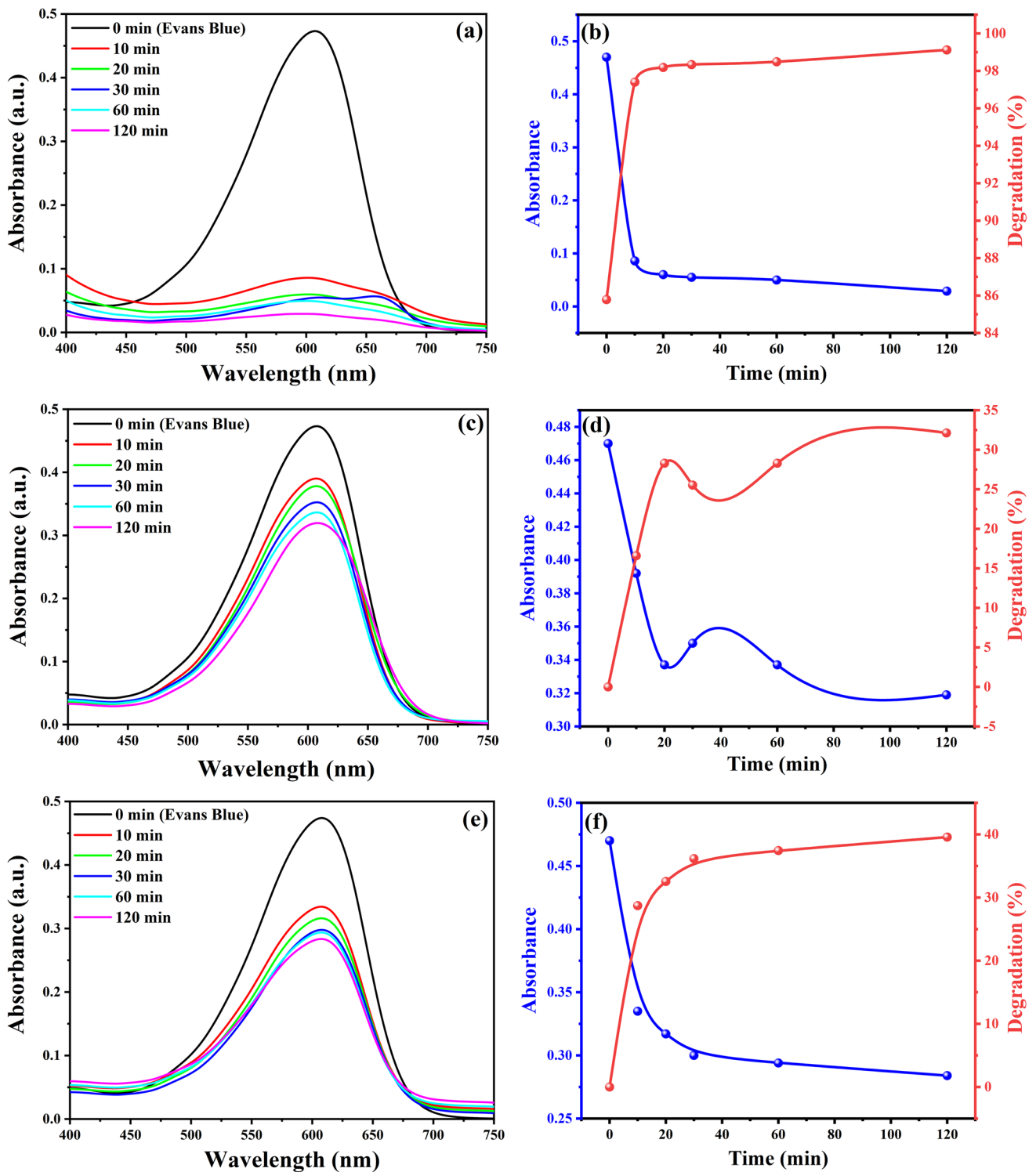


Fig. 8 Time effect reaction of iron oxide NPs on degradation of EB: (a) obtained by *Mentha Pulegium* L., (c) obtained by *Artemisia herba-alba*, (e) obtained by *Punica Granatum* L.); Degradation per-

cent degradation of EB (b) iron oxide NPs by *Mentha Pulegium* L., (d) iron oxide NPs by *Artemisia herba-alba*, (f) iron oxide NPs by *Punica Granatum* L.)

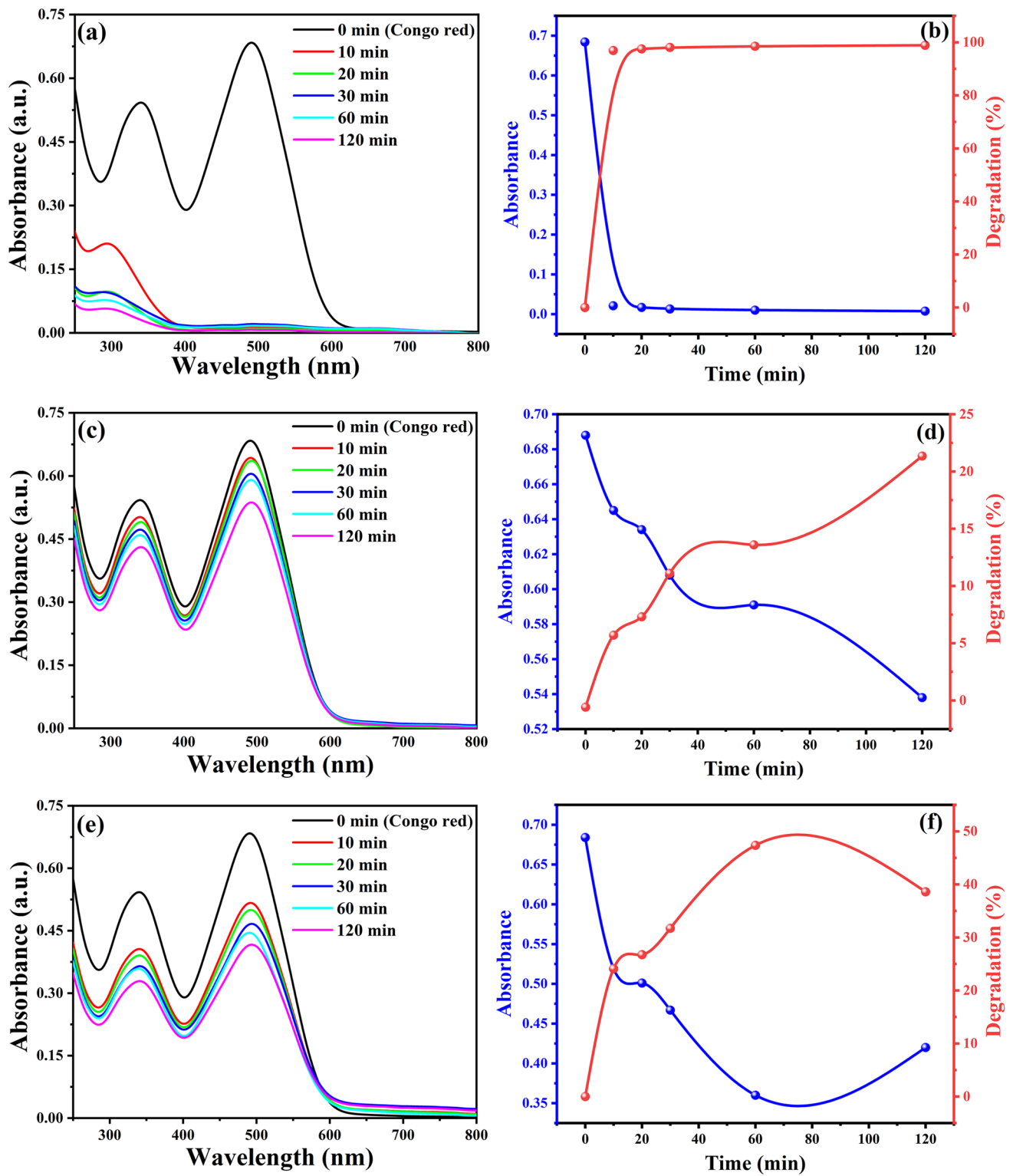


Fig. 9 Time effect reaction of iron oxide NPs on degradation of CR: (a) obtained by *Mentha Pulegium* L., (c) obtained by *Artemisia herba-alba*, (e) obtained by *Punica Granatum* L.; Degradation

percent degradation of CR (b) iron oxide NPs by *Mentha Pulegium* L., (d) iron oxide NPs by *Artemisia herba-alba*, (f) iron oxide NPs by *Punica Granatum* L.)

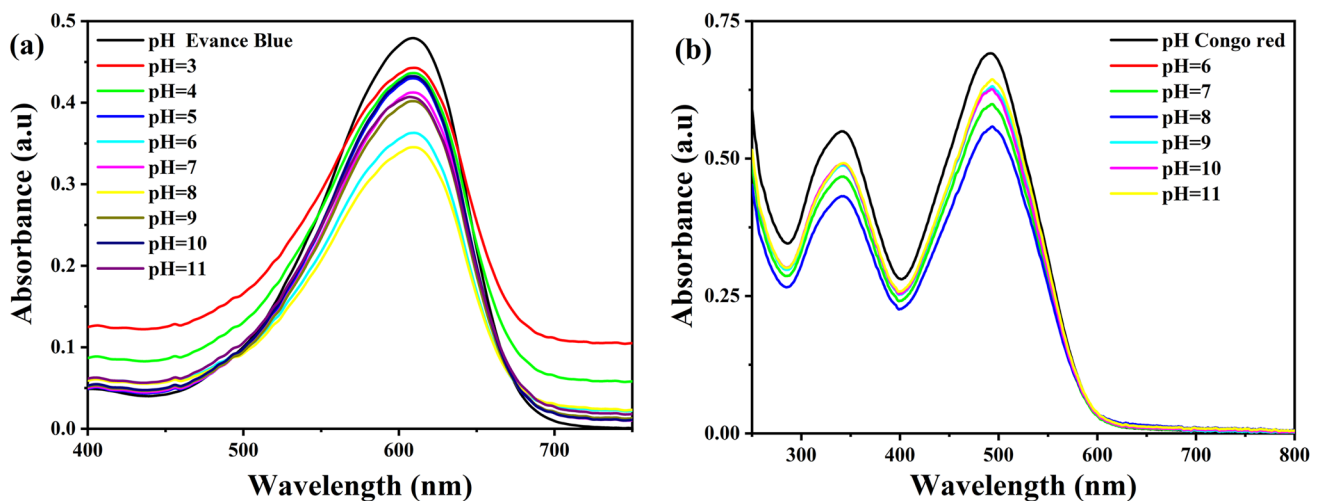


Fig. 10 Stability of Evans blue (a) and Congo red (b) in different pH value

4 Conclusion

In this study, that iron oxide nanoparticles manufactured using three different plants extracts create particles with distinct physical features that have a significant impact on sorption qualities. The process is relatively easy, fast, cheap, environmentally friendly, and does not require any organic solvents or other toxic reagents. Therefore, this synthesis method is more beneficial than conventional methods for the synthesis of Fe_3O_4 NPs. The shape of the prepared Fe_3O_4 NPs is close to spherical, the crystal in nature, and the average diameter is where the estimated size of *Mentha Pulegium* L, *Artemisia herba-alba*, and *Punica Granatum* L. crystallite sizes were 42.37, 31.68, 30.17 nm respectively. In addition, this study shows that the prepared Fe_3O_4 NPs have good catalytic activity for dye degradation of MB and CR stains under environmental conditions. The compound Fe_3O_4 NPs is proved to be useful in the treatment of wastewater (dye degradation) in medicines.

Author contribution Conceptualization, S.E.L., M.S., A.B., and H.H.; methodology, A.B., M.S., and M.L.T.; validation, A.B., S.E.L., M.S., and M.L.T.; investigation, A.B., M.L.T., and M.S.; resources, A.B.; data curation, A.B., M.L.T., and M.M.S.; writing—original draft preparation, S.E.L., M.S., A.B., H.H., M.L.T and B.D.; writing—review and editing, A.B., M.S., M.L.T, and, and H.H.; supervision, S.E.L., M.S., and H.H.; authors have read and agreed to the published version of the manuscript.

Data availability Not applicable.

Declarations

Conflict of interest The authors declare no competing interests.

References

- Abdi J, Vossoughi M, Mahmoodi NM, Alemzadeh I (2017) Synthesis of amine-modified zeolitic imidazolate framework-8, ultrasound-assisted dye removal and modeling. *Ultrason Sonochem* 39:550–564. <https://doi.org/10.1016/j.ultsonch.2017.04.030>
- Liu X, Li W, Chen N, Xing X, Dong C, Wang Y (2015) Ag–ZnO heterostructure nanoparticles with plasmon-enhanced catalytic degradation for Congo red under visible light. *RSC Adv* 5(43):34456–34465. <https://doi.org/10.1039/C5RA03143E>
- Tan IAW, Hameed BH, Ahmad AL (2007) Equilibrium and kinetic studies on basic dye adsorption by oil palm fibre activated carbon. *Chem Eng J* 127(1):111–119. <https://doi.org/10.1016/j.cej.2006.09.010>
- Yang D, Qiu L, Yang Y (2016) Efficient Adsorption of Methyl Orange Using a Modified Chitosan Magnetic Composite Adsorbent. *J Chem Eng Data* 61(11):3933–3940. <https://doi.org/10.1021/acs.jced.6b00706>
- Rath P, Priyadarshini B, Behera S, Parhi P, Panda S, Sahoo T (2019) Adsorptive removal of Congo Red dye from aqueous solution using TiO_2 nanoparticles: Kinetics, thermodynamics and isothermal insights. *AIP Conference Proceedings*: AIP Publishing LLC, p 030115
- Sinha T, Ahmaruzzaman M (2015) Green synthesis of copper nanoparticles for the efficient removal (degradation) of dye from aqueous phase. *Environ Sci Pollut Res* 22(24):20092–20100. <https://doi.org/10.1007/s11356-015-5223-y>
- Cuong HN, Pansambal S, Ghotekar S, Oza R, Hai NTT, Viet NM et al (2022) New frontiers in the plant extract mediated biosynthesis of copper oxide (CuO) nanoparticles and their potential applications: A review. *Environ Res* 203:111858
- Kouhbanani MAJ, Beheshtkhoo N, Taghizadeh S, Amani AM, Alimardani V (2019) One-step green synthesis and characterization of iron oxide nanoparticles using aqueous leaf extract of *Teucrium polium* and their catalytic application in dye degradation. *Adv Nat Sci Nanosci Nanotechnol* 10(1):015007
- Hamad HN, Idrus S (2022) Recent Developments in the Application of Bio-Waste-Derived Adsorbents for the Removal of Methylene Blue from Wastewater: A Review. *Polymers* 14(4):783
- Kangralkar MV, Kangralkar VA, Manjanna J (2021) Adsorption of Cr (VI) and photodegradation of rhodamine b, rose bengal and

- methyl red on Cu₂O nanoparticles. *Environ Nanotechnol Monitor Manag* 15:100417
11. Hussain MK, Khalid NR, Tanveer M, Kebaili I, Alrobei H (2021) Fabrication of CuO/MoO₃ p-n heterojunction for enhanced dyes degradation and hydrogen production from water splitting. *Int J Hydrogen Energy*. <https://doi.org/10.1016/j.ijhydene.2021.11.090>
 12. Ganesan K, Jothi VK, Natarajan A, Rajaram A, Ravichandran S, Ramalingam S (2020) Green synthesis of Copper oxide nanoparticles decorated with graphene oxide for anticancer activity and catalytic applications. *Arab J Chem* 13(8):6802–6814
 13. Kareem M, Bello I, Shittu H, Sivaprakash P, Adedokun O, Arumugam S (2022) Synthesis, characterization, and photocatalytic application of silver doped zinc oxide nanoparticles. *Clean Mater* 3:100041
 14. Lakshmanareddy N, Rao VN, Cheralathan KK, Subramaniam EP, Shankar MV (2019) Pt/TiO₂ nanotube photocatalyst—Effect of synthesis methods on valance state of Pt and its influence on hydrogen production and dye degradation. *J Colloid Interface Sci* 538:83–98
 15. Ardakani LS, Alimardani V, Tamaddon AM, Amani AM, Taghizadeh S (2021) Green synthesis of iron-based nanoparticles using *Chlorophytum comosum* leaf extract: Methyl orange dye degradation and antimicrobial properties. *Heliyon* 7(2):e06159
 16. Ba-Abbad MM, Takriff MS, Benamor A, Mohammad AW (2017) Size and shape controlled of α -Fe₂O₃ nanoparticles prepared via sol-gel technique and their photocatalytic activity. *J Sol-Gel Sci Technol* 81(3):880–893
 17. Beheshtkhou N, Kouhbanani MAJ, Savardashtaki A, Amani AM, Taghizadeh S (2018) Green synthesis of iron oxide nanoparticles by aqueous leaf extract of *Daphne mezereum* as a novel dye removing material. *Appl Phys A* 124(5):1–7
 18. Teja AS, Koh P-Y (2009) Synthesis, properties, and applications of magnetic iron oxide nanoparticles. *Prog Cryst Growth Charact Mater* 55(1–2):22–45
 19. Wang X (2011) Preparation of magnetic hydroxyapatite and their use as recyclable adsorbent for phenol in wastewater. *Clean-Soil, Air, Water* 39(1):13–20
 20. Jassal V, Shanker U, Gahlot S (2016) Green synthesis of some iron oxide nanoparticles and their interaction with 2-amino, 3-amino and 4-aminopyridines. *Mater Today Proc* 3(6):1874–1882
 21. Cornell RM, Schwertmann U (2003) The iron oxides: structure, properties, reactions, occurrences, and uses. Wiley-vch Weinheim
 22. Kumar R, Sen S (2013) Biogenic magnetite nanoparticles. *Res J Pharm Biol Chem Sci* 4(3):1037–1043
 23. Daniel-da-Silva AL, Trindade T, Goodfellow BJ, Costa BF, Correia RN, Gil AM (2007) In situ synthesis of magnetite nanoparticles in carrageenan gels. *Biomacromol* 8(8):2350–2357
 24. Belaiche Y, Khelef A, Laouini SE, Bouafia A, Tedjani ML, Barhoum A (2021) Green synthesis and characterization of silver/silver oxide nanoparticles using aqueous leaves extract of *Artemisia herba-alba* as reducing and capping agents. *Rev Rom Mater* 51(3):342–352
 25. Mihoc G, Ianoş R, Păcurariu C, Lazău I (2013) Combustion synthesis of some iron oxides used as adsorbents for phenol and p-chlorophenol removal from wastewater. *J Therm Anal Calorim* 112(1):391–397
 26. Drbohlavova J, Hrdy R, Adam V, Kizek R, Schneeweiss O, Hubalek J (2009) Preparation and properties of various magnetic nanoparticles. *Sensors* 9(4):2352–2362
 27. Özcan A, Oturan MA, Oturan N, Şahin Y (2009) Removal of Acid Orange 7 from water by electrochemically generated Fenton's reagent. *J Hazard Mater* 163(2):1213–1220. <https://doi.org/10.1016/j.jhazmat.2008.07.088>
 28. Abdullah JAA, Salah Eddine L, Abderrhmane B, Alonso-González M, Guerrero A, Romero A (2020) Green synthesis and characterization of iron oxide nanoparticles by pheonix *dactylifera* leaf extract and evaluation of their antioxidant activity. *Sustain Chem Pharm* 17:100280. <https://doi.org/10.1016/j.scp.2020.100280>
 29. Bouafia A, Laouini SE, Ouahrani MR (2020) A review on green synthesis of CuO nanoparticles using plant extract and evaluation of antimicrobial activity. *Asian J Res Chem* 13(1):65–70
 30. Abderrhmane B, Salah EL (2020) Plant-Mediated Synthesis of Iron Oxide Nanoparticles and Evaluation of the Antimicrobial Activity: A Review. *Mini-Rev Org Chem* 17:1–10. <https://doi.org/10.2174/1570193X17999200908091139>
 31. Bouafia A, Laouini SE, Khelef A, Tedjani ML, Guemari F (2020) Effect of Ferric Chloride Concentration on the Type of Magnetite (Fe₃O₄) Nanoparticles Biosynthesized by Aqueous Leaves Extract of *Artemisia* and Assessment of Their Antioxidant Activities. *J Cluster Sci*. <https://doi.org/10.1007/s10876-020-01868-7>
 32. Bouafia A, Laouini SE (2020) Green synthesis of iron oxide nanoparticles by aqueous leaves extract of *Mentha Pulegium* L.: Effect of ferric chloride concentration on the type of product. *Mater Lett* 265:127364. <https://doi.org/10.1016/j.matlet.2020.127364>
 33. Bouafia A, Laouini SE, Tedjani ML, Ali GAM, Barhoum A (2021) Green biosynthesis and physicochemical characterization of Fe₃O₄ nanoparticles using *Punica granatum* L. fruit peel extract for optoelectronic applications. *Text Res J*. <https://doi.org/10.1177/00405175211006671>
 34. Laouini SE, Bouafia A, Soldatov AV, Algarni H, Tedjani ML, Ali GAM et al (2021) Green Synthesized of Ag/Ag₂O Nanoparticles Using Aqueous Leaves Extracts of *Phoenix dactylifera* L. and Their Azo Dye Photodegradation. *Membranes* 11(7). <https://doi.org/10.3390/membranes11070468>
 35. Laid TM, Abdelhamid K, Eddine LS, Abderrhmane B (2021) Optimizing the biosynthesis parameters of iron oxide nanoparticles using central composite design. *J Mol Struct* 1229:129497. <https://doi.org/10.1016/j.molstruc.2020.129497>
 36. Bouafia A, Laouini SE, Ahmed ASA, Soldatov AV, Algarni H, Feng Chong K et al (2021) The Recent Progress on Silver Nanoparticles: Synthesis and Electronic Applications. *Nanomaterials* 11(9):2318
 37. Pillai PS, Prajapati DI, Ameta R, Ali Y (2016) Preparation of C-TiO₂ nanophotocatalyst and its used for degradation of evans blue. *Sci Revs Chem Commun* 6(1):12–18
 38. Hussein N, Nabeel Z (2018) Antimicrobial effects of *Mentha Pulegium* extract against *Staphylococcus Aureus* bacteria. *Al-Mustansiriyah J Sci* 29(2). <https://doi.org/10.23851/mjs.v29i2.155>
 39. Wright CW, *Artemisia* V (2002) Taylor & Francis. London and New York
 40. Laouini SE, Kelef A, Ouahrani MR (2018) Free radicals scavenging activity and phytochemical composition of *astermisia* (*Herba-Alba*) extract growth in Algeria. *J Fundam Appl Sci* 10(1):268–280
 41. Arul J, Sangeetha R (2015) Phytochemical screening of *Punica granatum* Linn. Peel extracts. *J Acad Indust Res* 4(5):160–162
 42. Nakagiri N, Manghnani MH, Ming LC, Kimura S (1986) Crystal structure of magnetite under pressure. *Phys Chem Miner* 13(4):238–244. <https://doi.org/10.1007/BF00308275>
 43. Pauling L, Hendricks SB (1925) THE CRYSTAL STRUCTURES OF HEMATITE AND CORUNDUM. *J Am Chem Soc* 47(3):781–790. <https://doi.org/10.1021/ja01680a027>
 44. Sakura GB, Leung AYT (2015) Experimental study of particle collection efficiency of cylindrical inlet type cyclone separator. *Int J Environ Sci Dev* 6(3):160
 45. Nm Izza, Dewi SR, Setyanda A, Sukoyo A, Utoro P, Al Riza DF et al (2018) Microwave-assisted extraction of phenolic compounds from *Moringa oleifera* seed as anti-biofouling agents in membrane processes. *MATEC Web Conf* 204:03003

46. Bello OS, Adegoke KA, Akinyunni OO (2017) Preparation and characterization of a novel adsorbent from *Moringa oleifera* leaf. *Appl Water Sci* 7(3):1295–1305. <https://doi.org/10.1007/s13201-015-0345-4>
47. Araújo CST, Melo EI, Alves VN, Coelho NMM (2010) *Moringa oleifera* Lam. seeds as a natural solid adsorbent for removal of AgI in aqueous solutions. *J Braz Chem Soc* 21:1727–32
48. Kanagasubbulakshmi S, Kadirvelu K (2017) Green synthesis of iron oxide nanoparticles using *Lagenaria siceraria* and evaluation of its antimicrobial activity. *Defence Life Sci J* 2(4):422–427
49. Shakil M, Inayat U, Khalid NR, Tanveer M, Gillani SSA, Tariq NH et al (2022) Enhanced structural, optical, and photocatalytic activities of Cd–Co doped Zn ferrites for degrading methyl orange dye under irradiation by visible light. *J Phys Chem Solids* 161:110419. <https://doi.org/10.1016/j.jpcs.2021.110419>
50. Shakil M, Inayat U, Arshad MI, Nabi G, Khalid NR, Tariq NH et al (2020) Influence of zinc and cadmium co-doping on optical and magnetic properties of cobalt ferrites. *Ceram Int* 46(6):7767–7773. <https://doi.org/10.1016/j.ceramint.2019.11.280>
51. Rafique M, Sohaib M, Tahir R, Tahir MB, Khalid NR, Shakil M et al (2021) Novel, facile and first time synthesis of zinc oxide nanoparticles using leaves extract of *Citrus reticulata* for photocatalytic and antibacterial activity. *Optik* 243:167495. <https://doi.org/10.1016/j.ijleo.2021.167495>
52. Tanveer M, Latif A, Nabi G, Shakil M, Khalid S, Qadeer MA (nd) *Carthamus oxycantha* extract derived novel green synthetic strategy for CaTiO₃ nano-structures displaying an enhanced photo-degradation for a mixture of dyes (MB+RHB) and antibacterial activity. Available at SSRN: <https://ssrn.com/abstract=3999212> or <https://doi.org/10.2139/ssrn.3999212>
53. Soni V, Khosla A, Singh P, Nguyen V-H, Le QV, Selvasembian R et al (2022) Current perspective in metal oxide based photocatalysts for virus disinfection: A review. *J Environ Manage* 308:114617. <https://doi.org/10.1016/j.jenvman.2022.114617>
54. Abdulkadir I, Abdallah HMI, Jonnalagadda SB, Martincigh BS (2018) The effect of synthesis method on the structure, and magnetic and photocatalytic properties of hematite (α -Fe₂O₃) nanoparticles. *S Afr J Chem* 71:68–78
55. Sharp EL, Jarvis P, Parsons SA, Jefferson B (2006) Impact of fractional character on the coagulation of NOM. *Colloids Surf, A* 286(1):104–111. <https://doi.org/10.1016/j.colsurfa.2006.03.009>
56. Groiss S, Selvaraj R, Varadavenkatesan T, Vinayagam R (2017) Structural characterization, antibacterial and catalytic effect of iron oxide nanoparticles synthesised using the leaf extract of *Cynometra ramiflora*. *J Mol Struct* 1128:572–578. <https://doi.org/10.1016/j.molstruc.2016.09.031>
57. Gosens I, Post JA, de la Fonteyne LJJ, Jansen EHJM, Geus JW, Cassee FR et al (2010) Impact of agglomeration state of nano- and submicron sized gold particles on pulmonary inflammation. *Part Fibre Toxicol* 7(1):37. <https://doi.org/10.1186/1743-8977-7-37>
58. Karpagavinayagam P, Vedhi C (2019) Green synthesis of iron oxide nanoparticles using *Avicennia marina* flower extract. *Vacuum* 160:286–292
59. Groiss S, Selvaraj R, Varadavenkatesan T, Ramesh V (2016) Structural characterization, antibacterial and catalytic effect of iron oxide nanoparticles synthesised using the leaf extract of *Cynometra ramiflora*
60. Liao C, Li Y, Tjong SC (2020) Visible-Light Active Titanium Dioxide Nanomaterials with Bactericidal Properties. *Nanomaterials* 10(1):124
61. Jayakumarai G, Gokulpriya C, Sudhapriya R, Sharmila G, Muthukumaran C (2015) Phytofabrication and characterization of monodisperse copper oxide nanoparticles using *Albizia lebeck* leaf extract. *Appl Nanosci* 5(8):1017–1021. <https://doi.org/10.1007/s13204-015-0402-1>
62. Lassoued A, Lassoued MS, Dkhil B, Ammar S, Gadri A (2018) Synthesis, structural, morphological, optical and magnetic characterization of iron oxide (α -Fe₂O₃) nanoparticles by precipitation method: effect of varying the nature of precursor. *Physica E* 97:328–334
63. Soltan WB, Nasri S, Lassoued MS, Ammar S (2017) Structural, optical properties, impedance spectroscopy studies and electrical conductivity of SnO₂ nanoparticles prepared by polyol method. *J Mater Sci: Mater Electron* 28(9):6649–6656
64. Beranek R, Kisch H (2008) Tuning the optical and photoelectrochemical properties of surface-modified TiO₂. *Photochem Photobiol Sci* 7(1):40–48
65. Ali GAM, Thalji MR, Soh WC, Algarni H, Chong KF (2020) One-step electrochemical synthesis of MoS₂/graphene composite for supercapacitor application. *J Solid State Electrochem* 24(1):25–34. <https://doi.org/10.1007/s10008-019-04449-5>
66. Naeimi A, Sharifi A, Montazerghaem L, Abhari AR, Mahmoodi Z, Bakr ZH et al (2022) Transition metals doped WO₃ photocatalyst towards high efficiency decolourization of azo dye. *J Mol Struct* 1250:131800. <https://doi.org/10.1016/j.molstruc.2021.131800>
67. Strehlow WH, Cook EL (1973) Compilation of Energy Band Gaps in Elemental and Binary Compound Semiconductors and Insulators. *J Phys Chem Ref Data* 2(1):163–200. <https://doi.org/10.1063/1.3253115>
68. Kulkarni SA, Sawadh PS, Palei PK, Kokate KK (2014) Effect of synthesis route on the structural, optical and magnetic properties of Fe₃O₄ nanoparticles. *Ceram Int* 40(1, Part B):1945–9. <https://doi.org/10.1016/j.ceramint.2013.07.103>
69. Ali GAM, Yusoff MM, Ng YH, Lim HN, Chong KF (2015) Potentiostatic and galvanostatic electrodeposition of manganese oxide for supercapacitor application: A comparison study. *Curr Appl Phys* 15(10):1143–1147. <https://doi.org/10.1016/j.cap.2015.06.022>
70. Martienssen W (1957) Über die excitonenbanden der alkalihalogendkristalle. *J Phys Chem Solids* 2(4):257–267. [https://doi.org/10.1016/0022-3697\(57\)90070-7](https://doi.org/10.1016/0022-3697(57)90070-7)
71. Ethiraj AS, Uttam PKV, Chong KF, Ali GAM (2020) Photocatalytic performance of a novel semiconductor nanocatalyst: Copper doped nickel oxide for phenol degradation. *Mater Chem Phys* 242:122520. <https://doi.org/10.1016/j.matchemphys.2019.122520>
72. Sharifi A, Montazerghaem L, Naeimi A, Abhari AR, Vafae M, Ali GAM et al (2019) Investigation of photocatalytic behavior of modified ZnS:Mn/MWCNTs nanocomposite for organic pollutants effective photodegradation. *J Environ Manage* 247:624–632. <https://doi.org/10.1016/j.jenvman.2019.06.096>
73. Giahi M, Pathania D, Agarwal S, Ali GAM, Chong KF, Gupta VK (2019) Preparation of Mg-doped TiO₂ nanoparticles for photocatalytic degradation of some organic pollutants. *Stud Univ Babeş-Bolyai, Chem* 64(1):7–18
74. Pang YL, Law ZX, Lim S, Chan YY, Shuit SH, Chong WC et al (2021) Enhanced photocatalytic degradation of methyl orange by coconut shell-derived biochar composites under visible LED light irradiation. *Environ Sci Pollut Res*. <https://doi.org/10.1007/s11356-020-12251-4>
75. Khalid NR, Arshad A, Tahir MB, Hussain MK (2021) Fabrication of p–n heterojunction Ag₂O@Ce₂O nanocomposites make enables to improve photocatalytic activity under visible light. *Appl Nanosci* 11(1):199–206. <https://doi.org/10.1007/s13204-020-01571-z>

76. Khalid NR, Hussain MK, Murtaza G, Ikram M, Ahmad M, Hammad A (2019) A Novel Ag₂O/Fe–TiO₂ Photocatalyst for CO₂ Conversion into Methane Under Visible Light. *J Inorg Organomet Polym Mater* 29(4):1288–1296. <https://doi.org/10.1007/s10904-019-01092-5>
77. Ghorai TK (2011) Photocatalytic Degradation of 4-chlorophenol by CuMoO₄-doped TiO₂ Nanoparticles Synthesized by Chemical Route. *Open J Phys Chem* 01(02):9. <https://doi.org/10.4236/ojpc.2011.12005>
78. Fu L, Wu Y-n, Li F, Zhang B (2013) Synthesis of InNbO₄ short nanofiber membrane as visible-light-driven photocatalyst. *Mater Lett* 109:225–8. <https://doi.org/10.1016/j.matlet.2013.07.096>
79. Azeez F, Al-Hetlani E, Arafa M, Abdelmonem Y, Nazeer AA, Amin MO et al (2018) The effect of surface charge on photocatalytic degradation of methylene blue dye using chargeable titania nanoparticles. *Sci Rep* 8(1):7104. <https://doi.org/10.1038/s41598-018-25673-5>

Publisher's note Springer Nature remains neutral with regard to jurisdictional claims in published maps and institutional affiliations.